Reconciling fracture toughness parameter contradictions in thin ductile metal sheets in tension

Wade R Lanning[1], Syed S Javaid[2], and Christopher L Muhlstein [11]

[1]School of Materials Science and Engineering, Georgia Institute of Technology USA

[1]Christopher Muhlstein, School of Materials Science and Engineering, Georgia Institute of Technology, 771 Ferst Dr NW, Atlanta, GA 30332 USA
email: christopher.muhlstein@mse.gatech.edu

Abstract

The well-known trade-off between strength and fracture toughness in bulk specimens is often used to explain the low fracture toughness of very thin ductile face-centered cubic (FCC) metal specimens, but this interpretation contradicts the relative length scales of thickness-dependent strength and thickness-dependent fracture toughness. This study uses the concept of similitude to demonstrate that linear elastic fracture mechanics (LEFM) analysis of 25.4 μm thick annealed aluminum is invalid, though the resulting fracture toughness measurements fit well with the existing literature and idea of a strength/fracture toughness trade-off. Similarly, a elastic plastic fracture mechanics (EPFM) analysis is sensitive to out-of-plane deformation which cannot be practically eliminated or corrected for with a model. However a plastic collapse analysis using a critical net section stress criterion is demonstrably valid by the concept of similitude, is insensitive to out of plane deformation, and agrees with the evidence of extensive plasticity in the fracture surfaces.

Keywords fracture toughness, plastic collapse, thin sheet, ductile tearing, stable crack growth, fracture mechanics

Introduction

Face-centered cubic (FCC) metal nanospecimens have remarkably low reported fracture toughnesses, in some cases with $K_{Ic} = 1\,\mathrm{MPa}\sqrt{\mathrm{m}}$ or lower for films $\approx 100\,\mathrm{nm}$ thick.[1–3] One popular explanation of the apparently low fracture toughness of thin FCC metal specimens is that the increased yield strength observed in nanopillars in compression[4–6] and nanopillars[6] and films[6–10] in tension causes the low fracture toughness of thin specimens[1,2,7,10] just like the strength/fracture toughness trade-off seen in larger-scale specimens.[11] However, upon closer inspection it becomes apparent that size-induced strengthening is a phenomenon observed primarily in sub-micron specimens[4–10,12] while decreasing fracture toughness with specimen size can be observed at much larger length scales.[13–17] Consequently, the low fracture toughnesses observed in thin ductile metal sheets must be a consequence of an inappropriate analysis for the thin sheets and/or thickness limiting the strength of the sheets by means other than the strength/fracture toughness trade-off observed in the bulk.[18]

Work exploring the low fracture toughness ultrathin specimens is relatively recent,[1–3] but the phenomenon of specimen size-dependent fracture toughness has been a prominent subject since the early days of fracture mechanics research.[13,15,16,19] Fig. 1 qualitatively shows the relationship between fracture toughness and specimen thickness B for a ductile metal. While the increase in fracture toughness with decreasing thickness below the minimum thickness B^0 of the plane strain regime is well-known,[19] the regime of thickness-limited fracture toughness exhibited by some metals at thicknesses below the critical thickness B^* often goes unacknowledged. Below B^* fracture of ductile metals proceeds by localized thickness reduction at the crack tip (transverse necking). Because the length scale of the transverse neck scales with the thickness, the fracture toughness also decreases with decreasing thickness and can descend below the plane strain fracture toughness for very thin specimens.[20] Thus the low fracture toughnesses of very thin FCC metal sheets[4–10,12]

are not necessarily due to changes in material properties, but may instead be consequences of geometric effects on the fracture process.[20,21]

Unlike specimen size-dependent strength,[12] size-dependent fracture toughness in thin FCC metal specimens is not a phenomenon particular to the nanoscale.[15,16] The length scale regime of specimen size-induced strengthening is limited to very small specimens (a few μm or thinner[4–10,12]), but the fracture toughness of FCC metals has been shown to begin decreasing below a critical thickness B^* as large as a few mm.[13–17] For example, Kang et al. found the onset of decreasing fracture toughness below a critical thickness B^* of 300 μm for pure copper foils[15] while other studies found the onset of increasing strength with decreasing thickness begins around 1 μm and thinner.[9,10,12] Similarly, the fracture toughness of aluminum 7075-T6 begins to decrease with decreasing thickness at thicknesses of 1 mm and below[16]), but significant thickness-dependent strengthening only appears at thicknesses of a few μm and below.[9] Additionally, the same high-strength nanospecimens cited earlier exhibited extensive dislocation-mediated plasticity, plastic strains before failure, and ductile fracture.[4–6,22,23] Therefore it does not follow that the low fracture toughness measured in thin ductile metal sheets[1,2,7,10,15] is due to brittle fracture as some might infer based on trends in the bulk. Instead, the low fracture toughness measurements must be a consequence of thickness-limited ductile crack growth, selection of fracture toughness parameters unsuited to thin ductile metal sheets, or both. This study discusses how one may determine the applicability of fracture toughness parameters using comparisons between experiments performed using specimens of the same thickness but different in-plane geometries.

Published work on the fracture toughness of thin FCC metal sheets, like prior studies of bulk systems, favors two approaches: the linear-elastic fracture mechanics (LEFM) parameter K,[1–3] and the elastic-plastic fracture mechanics (EPFM) parameter J.[15] A fracture toughness measurement is only meaningful if the test specimens behave in a manner consistent with the theory upon which the fracture toughness parameter is based, which gives rise to the concept of "validity" criteria for different parameters.[24,25] In the case of both K and J the validity criteria take the form of the minimum specimen dimensions that ensure the near-crack tip process zone is contained in a volume

small relative to the rest of the specimen. The nomenclature "-dominated" and "-controlled" are used to denote when a particular crack tip parameter is applicable. In other words there are minimum specimen dimensions for which a specimen may be considered K-dominated, and another set of smaller minimum dimensions for J-dominance.[24,26] The validity criteria of K and J are based upon the concept of "similitude"; which we define as when a measured value of a fracture toughness parameter consistently describes the conditions necessary to drive crack growth independent of starting crack length or specimen geometry.[18] In fact, demonstrating similitude (or the absence of similitude's counterpart "uniqueness") was core to the development of the K, J, and unified fracture toughness measurement validity criteria of the ASTM standards.[24,25,27] Thin ductile FCC metal sheets violate standardized validity criteria by virtue of their thinness, so we must use tools like similitude tests to determine which fracture toughness parameters are applicable to a given thin FCC ductile metal sheet.[18,25,28] Additionally, we must consider the possibility that establishing K-dominance or J-dominance in thin ductile metal specimens may require prohibitively large specimens, and an alternative parameter will be needed. After all, a fracture toughness measurement which can only be reproduced in very large specimens is practically useless if the system being characterized only ever sees service in smaller-scale components.

If we consider the nature of traditional LEFM and EPFM in the context of small specimen testing, we can find additional reasons to rethink how we measure fracture toughness in small ductile metal specimens. First, the LEFM and EPFM fracture toughness parameters are only valid above a minimum specimen size, which calls into question any measurement of fracture toughness small specimens of ductile metals. Secondly, the morphology of plastic deformation at the tip of cracks in small specimens is different from the thicker specimens upon which LEFM and EPFM validity criteria are based. The shape and extent of the crack tip plastic zones of ductile FCC metal thin sheets varies with thickness.[7,10,15,29,30] Classic studies showed shifts in plastic zone morphology at the transition from plane strain to plane stress in metal specimens a few mm in thickness,[29,30] while more recent work in nanoscale ductile metal sheets show crack tip plastic zones which vary with texture and defect configurations near the crack tip.[7,10,15] Furthermore, Keller et al. demon-

strated that even nanograined copper sheets, which show little to no plastic deformation prior to failure in uniaxial tension, can exhibit significant dislocation activity near a crack tip.[7] Adaptation of conventional LEFM and EPFM validity criteria to small ductile metal specimens would require an understanding of crack tip plasticity at the nanoscale-beyond the current state of the art. Instead, this study applies the concept of similitude to determine whether LEFM, EPFM, or a large scale plasticity crack tip parameter best describes crack growth in a set of ductile metal thin sheets.

Materials and Methods

Specimens were fabricated from annealed 25.4 μm thick 1235 aluminum (minimum aluminum content 99.35 %) foil stock purchased from McMaster-Carr. The dogbone-style specimens were cut on a Sizzix eclips2 electronic cutter based on the ASTM E345 A geometry.[31] Specimens were all fabricated with the same gauge length (20 mm) and fillet radius (9.5 mm), but were made in two different total widths: 6.25 mm in width referred to as "single-width" or "SW" in all data sets shown here and 12.5 mm in width referred to as "double-width" or "DW." Notches from 1.0 mm to 3.0 mm in total length were cut at the midpoint of the gauge length using either the electronic cutter (which uses a blade) or a QuikLaze-50ST2 machining laser. The laser was operated with the 100x objective, 30 Hz pulse rate, a 20 μm by 4 μm exposure area, and set at 100 % of the high power setting of the 355 nm IR wavelength. Specimens were fabricated as either single edge notch tension "SE(T)" or middle crack tension "M(T)." Notches for M(T) specimens must be cut as precisely in the center of the specimen as possible and with identical notch tip conditions, so all center notches were cut with the laser. Three different initial SE(T) notch types were used in order to compare their effect on fracture toughness: laser-cut notches, blade-cut notches, and laser-cut notches with fatigue precracks. Precracking is meant to achieve three objectives: a sharp crack tip, small cyclic plastic zone, and long enough precrack to escape the influence of the notch (which scales with the notch radius). Rather than attempting to apply standard procedures based on crack tip parameters which may or may not be valid for our ductile thin sheets,[24,27] we developed a method for growing long sharp precracks with relatively small crack tip plastic zones. We applied

half of the force necessary to grow a crack from a laser-cut notch to ensure that the cyclic plastic zone was small relative to that developed by a fracture toughness test. Fatigue precracks were grown by applying 100,000 cycles with a sawtooth waveform at half of the critical stress observed for for the crack growth of notched specimens. The load ratio was held constant during precracking at $R = \sigma_{max}/\sigma_{min} = 0.1$ where σ_{max} is the maximum stress and σ_{min} is the minimum stress during each cycle (not to be confused the "*R*" in the phrase "*K*-*R* curve"). The resulting fatigue precracks were quite sharp and long relative to the starting notch tip radius. For example two specimens with starting notch length 3 mm were cycled between 6 N and 0.6 N for 100,000 cycles, resulting in roughly 200 µm of fatigue crack growth from the 2.5 µm diameter laser-cut notch tip. If LEFM was applicable to these specimens, then the plastic zone size of these specimens would be 1/4 the size of the plastic zone developed during a fracture toughness experiment.

In order to ensure that all specimens remained flat with minimal wrinkling or slack in the sheet, specimens were placed onto copy paper backings before being fixed in the load frame grips. Only the grip sections of the specimens were glued down, while the gauge and fillet sections were laid flat on the paper backing but were otherwise free. Once the specimen was aligned and fixed on the load frame grips, the backing behind the gauge section (which had been perforated in advance on the electronic cutter) was torn away. Some specimens of both the SE(T) and M(T) geometries were also tested with anti-buckling plates in place. These specimens were sandwiched between two glass slides (the anti-buckling plates) cut to a length so as to cover the bottom grip section and gauge section of the specimen, but not the top grip section. The bottom grip section which lay between the glass slides had an extra layer of the 25.4 µm 1235 aluminum foil on either side to act as a spacer and prevent the glass slides from contacting the gauge section unless it buckled. During testing, the bottom grip section was gripped between the anti-buckling glass slides which were in turn squeezed within the vise grip while the top grip section was gripped directly by the vise grips. Though the anti-buckling plates do not completely suppress buckling, they reduce out of plane deflection and push the buckling mode from the third harmonic to higher order harmonics. This is because the space between the specimen and anti-buckling plates allowed for some buckling

to occur, and that space had to be left in order to minimize the effects of friction between the anti-buckling plates and the specimens.

All specimens (SE(T), M(T), blade-cut notches, laser-cut notches, fatigue precracked, with anti-buckling plates and without) were then tested in tension using an Instron 5848 mechanical test frame with vise grips and a 100 N Instron 2530-427 static load cell. A 3.1 megapixel (2048 x 1536) PixeLink CCD camera fitted with a 2x magnification Mitutoyo microscope objective lens was used to capture images across the width of the specimen prior to testing in order to measure the initial notch length and assist in later crack length measurements. A computer using a custom-built program written in NI Labview 7.1 used a GPIB interface to both control the load frame and record logged force and displacement data. All tests were performed in displacement control at a rate of 0.1 mm per minute while simultaneously capturing backlit images of the crack tip at 1 second integrals using the 3.1 megapixel camera triggered by a HP 33120A function generator synchronized to the beginning of the test. The images captured during the experiment were then used to measure the crack length to within the spatial resolution of the camera and optics (1.8 μm) during the experiment. The experiments were stopped and resumed after each $\approx$1.0 mm increment of crack growth to move the camera to recenter the camera on the crack tip. The M(T) specimens were also imaged across the entire length of the crack at before re-starting the experiment to verify equal growth of both crack fronts. The experiments were stopped when the cracks either reached the far edge of the specimens or a secondary crack initiated from the back edge. Representative fracture surfaces were imaged using a Hitachi TM3030 bench-top scanning electron microscope (SEM) in "shadow" backscatter imaging mode.

Values of the linear elastic stress intensity factor K were computed for the portions of each tensile experiment in which crack growth was apparent in the images captured. Both SE(T) and M(T) stress intensity factors were simulated by finite element (FE) models in ANSYS Mechanical APDL 15.0 for a range of crack lengths. Both the SW (6.25 mm wide) and DW (12.5 mm wide) SE(T) specimens required a specially-computed K solution due to the effects of the grips providing a reaction moment which increases with crack opening and crack length. M(T) specimens are

symmetric about their center axis, so the grips at the specimen ends produce no reaction moment to crack opening like the SE(T) specimens. As a result, our ANSYS K solutions for M(T) specimens match those from *The Stress Analysis of Cracks Handbook*.[32] The K solutions are all of the form $K = \sigma Y\sqrt{\pi a}$ where a is the crack length, σ is the stress computed using the total specimen width w and thickness B of the gauge cross section, and Y is a geometric term specific to the specimen configuration and a function of $\frac{a}{w}$. The geometric term Y from the FE solution for a SW (6.25 mm wide) SE(T) specimen was fit by linear regression in *Mathematica* 10 to a polynomial, giving Eqn. 1.

$$Y = 1.12 - 1.54\left(\frac{a}{w}\right) + 30.80\left(\frac{a}{w}\right)^2 - 146.63\left(\frac{a}{w}\right)^3 + 341.81\left(\frac{a}{w}\right)^4 - 365.38\left(\frac{a}{w}\right)^5 + 145.67\left(\frac{a}{w}\right)^6 \tag{1}$$

Eqn. 2 gives the polynomial fit to the FE models' K solution for a DW (12.5 mm wide) SE(T) specimen.

$$Y = 1.12 - 1.63\left(\frac{a}{w}\right) + 30.13\left(\frac{a}{w}\right)^2 - 151.06\left(\frac{a}{w}\right)^3 + 353.11\left(\frac{a}{w}\right)^4 - 379.93\left(\frac{a}{w}\right)^5 + 153.85\left(\frac{a}{w}\right)^6 \tag{2}$$

Eqn. 3 gives the K solution for a M(T) specimen from *The Stress Analysis of Cracks Handbook*[32] which agrees with the FE simulations of both the M(T) SW (6.25 mm wide) and M(T) DW (12.5 mm wide). The agreement is because symmetric M(T) specimens produce no gross specimen rotation with crack opening, and thus there is no reaction moment from the grips or dependence on the non-gauge section portions of the specimen geometry.

$$Y = \left(1 - 0.025\left(\frac{a}{w}\right)^2 + 0.06\left(\frac{a}{w}\right)^4\right)\sqrt{\sec\left(\frac{\pi a}{2w}\right)} \tag{3}$$

Fig. 3 shows the output from the ANSYS simulations along with lines for the curve fits to the SE(T) solutions and the handbook[32] M(T) solution. It is important to note that though *The*

Stress Analysis of Cracks Handbook contains solutions for SE(T) specimens, those solutions are for specimens which experience a distributed tensile stress at both ends and are free to rotate with crack opening with *no reaction moments from fixed grips*.[32] SE(T) specimens held by fixed grips are influenced by constraints imposed by those grips. The degree of influence of the grips on the LEFM stress intensity factor K depends on crack length and specimen aspect ratio as discussed in greater detail later in this study.

K-based toughness measurements of the foils were computed in the form of K-R curves which show the nominal stress intensity K necessary to propagate a crack as a function of crack length a for SE(T) specimens or $2a$ for M(T) specimens across a specimen of width w or $2w$, respectively. However the ASTM standards for determination of fracture toughness,[24] stable tearing,[33] and K-R curves[27] give no clear distinction between the initiation and propagation stages of crack growth. Thus, we chose a method based on the ASTM aluminum tearing standard B871 to quantify the "initiation toughness" of our thin aluminum sheets. B871 defines "initiation" as the portion of the experiment preceding the maximum stress measured during the experiment and "propagation" as the remaining portion of the experiment following the maximum force.[34] Thus, we defined the initiation toughness as the toughness corresponding to the maximum force measured during the experiment.

A plastic collapse crack propagation toughness was measured from plots of the nominal stress σ plotted as a function of the ratio of cracked cross-section to total cross-section of the specimens, a/w. Data from all of the specimens tested was plotted on the σ vs a/w including only the data for crack propagation from the starting notch or fatigue precrack, Δa, greater than 125 µm. Then a linear least squares fit was applied to the data in Wolfram *Mathematica* 10 was applied to the data and forced to intercept the a/w-axis at $a/w = 1$. The collapse propagation toughness σ_c was taken from the σ-axis intercept at $a/w = 0$.

Additionally, a uniaxial tensile test was performed on a 12.5 mm wide "DW" specimen cut with from the as-received 1235 aluminum roll with a QuikLaze-50ST2 machining laser using the same parameters used to cut notches noted above. This test was performed in displacement control

at a rate of $0.1\,\mathrm{mm\,min^{-1}}$ on an Instron 5848 mechanical test frame with vise grips and a 100 N Instron 2530-427 static load cell. Image capture was performed during the experiment using a 5.0 megapixel (2592 x 1944) PixeLink CCD camera fitted with a 2x magnification Mitutoyo microscope objective lens synchronized to the beginning of the experiment by a HP 33120A function generator and capturing images at 0.5 Hz. Strain was computed using a digital image correlation and tracking (DICT) program running in Python 2.7 and synchronized to the timestamped force data to compute a stress-strain curve. The first 0.03 % strain was fitted by least squares, and the intercept of that line with the stress axis used to account for the preload on the specimen. The fitted line was then offset by 0.2 % strain to compute the yield strength (offset = 0.2 %) consistent with ASTM E8.[35]

The annealed 1235 aluminum sheets were electropolished, anodized, and imaged with polarized light microscopy to reveal the in-plane grain structure. Should the reader wish to perform similar metallographic preparation, we recommend Vander Voort's excellent metallography text.[36] Roughly 10 cm by 10 cm panels were cut directly from the roll with scissors, and then Kapton tape was applied to one side. The panels were then cut into approximately 1.5 cm by 4 cm strips, and an additional 1 cm wide piece of Kapton tape was applied across the center of each strip, leaving two $\approx$1.5 cm by 1 cm rectangular regions of foil exposed on each end of the strip. The area to be polished was measured with digital calipers. The strips were gripped at one end by an alligator clip spaced 1 cm from a 4 cm wide by 6 centimetre tall cathode cute from the same aluminum stock. The electrolyte (49 ml phosphoric acid, 47 ml ethanol, and 104 ml deionized water) was mixed an placed in a 250 ml glass beaker in a VWR water bath held at 45 ° °C. The specimen (anode) and cathode were placed so that the specimen was immersed halfway (roughly 2.5 cm) in the electrolyte and the portion of the specimen in contact with the electrolyte surface was completely protected by Kapton tape. Then an Agilent E-3612A power supply was used to apply $100\,\mathrm{mAcm^{-2}}$ to the specimen for 4 min 30 s while the operator gently tapped on the specimen holder approximately once per second to knock loose any gas bubbles which formed. The specimens were then rinsed in warm water and anodized for 20 s in a 2.3 % fluoroboric acid solution at 20 ° °C with a current

density of 155 $mAcm^{-2}$ (using the same setup with a fresh electrode) before being rinsed in warm water again.

The anodized specimens were then imaged using an Olympus BX40 optical microscope in bright field mode using the 5× objective and two (U-PO and U-AN360) polarization filters. Anodization creates a thin oxide layer epitaxial to the underlying metal crystals which gives contrast to the individual grains when viewed with polarized light microscopy.[36] Twenty lines were overlaid onto the resulting micrograph with random positions and orientations, and the number of intercepts between each line and the grain boundaries were manually counted. The 20 randomly placed lines resulted in more than 500 intercepts, which is in excess of the minimum recommendation for approximating grain size in ASTM E112.[37]

Phase analysis and texture studies were carried out using a PANalytical X?Pert MRD Pro diffractometer in parallel beam geometry with Cu-Kα radiation through a sealed Cu tube (45 kV/40 mA) and a graphite monocromater, a polycapillary X-Ray lens (1 mm × 1 mm), an Eulerian cradle and a proportional counter. Error sources such as specimen displacement, defocusing and peak shape ? size anomalies were avoided using parallel beam geometry (foil collimators as secondary optics). Glancing angle measurements were utilized to capture the surface and through thickness texture of the 25.4 µm aluminum sheet. An ω value of 5° was chosen for a penetration depth of 22 µm capturing the through thickness texture while a 2° value was chosen for a penetration depth of 10 µm. An open source MATLAB program MTEX v.4.3 was used to analyze the texture data obtained and generate pole figures and inverse pole figures.

Results and Discussion

All of the cracks in the specimens tested (SE(T) and M(T) of various widths) grew stably in displacement-control tensile experiments. The fracture surfaces (Fig. 2) were consistent with ductile crack growth with through-thickness (i.e. transverse) necking down to a point before separation. The fracture surfaces showed the same characteristics after a transition region that extended from a distance approximately equal to the sheet thickness from the starting notch (≈25 µm as seen

in Fig. 2A and 2B) until the crack reached the back edge. The fracture surfaces of SE(T) and M(T) specimens of different widths were also nominally the same. All of the fracture surfaces showed signs of transverse plastic necking down to a fine point before final separation (Fig. 2). The initial analysis of crack growth in these 25.4 μm thick 1235 aluminum sheets is straightforward: crack growth occurred by stable propagation of a through-thickness plastic neck just as one would expect for a highly ductile metal in plane stress.[38] Furthermore, the similarity between SE(T) and M(T) fracture surface for all crack lengths suggests similitude between the crack growth processes for all of the crack lengths and specimen geometries tested.

In the course of developing the K analysis for the specimens used in this study, it became apparent that there is a major discrepancy between the stress intensity solutions applied to SE(T) specimens in the literature[1,2,10,39] and the stress intensity of the actual experimental configurations which are commonly used. Fig. 4 shows the difference in the geometric factors Y used by various sources in the literature, most of which are comparable to those computed by Tada et al. and published in *The Stress Analysis of Cracks Handbook*.[32] The problem is that the Tada's solutions are for uniform stress boundary conditions, but a gripped specimen has uniform displacement boundary conditions (presuming the grips are torsionally rigid). In other words, the opening of an edge crack in tension results in a rotation of the specimen ends. Fixed grip conditions like those used in this study and[1,2,10,39] provide a reaction moment which reduces the stress intensity, relative to a specimen with ends left free to rotate. As crack length increases, the error between the uniform stress boundary condition K solutions (no reaction moment) SE(T) solutions and the solutions which account for the test fixture's uniform displacement boundary conditions increases dramatically. Fig. 3 shows the error between the uniform displacement and uniform stress boundary conditions as well as some examples of publications which applied the uniform stress solution to a uniform displacement boundary condition experiment.[1,2,10,39] The error increases with decreasing specimen aspect ratio ($\frac{\text{specimen length}}{\text{specimen width}}$) and increasing crack length a. The error manifests as an overestimation of the stress intensity K because the reduction of K by a reaction moment at the uniform displacement boundaries is not accounted for. Even for those cases where K is a valid

crack tip parameter, failure to account for boundary conditions results in significant errors in the calculation of fracture toughness.

If we perform only a cursory comparison of the different width SE(T) specimens' *K*-*R* curves (Fig. 5), the LEFM-based data analysis seems plausible at first. The initiation toughnesses defined by the maximum stress measured during the experiment are very similar. The SW SE(T) specimens had an average initiation toughness of $3.89 \pm 0.90\,\mathrm{MPa}\sqrt{\mathrm{m}}$ compared to $3.72 \pm 0.56\,\mathrm{MPa}\sqrt{\mathrm{m}}$ for DW SE(T) specimens. Both the SW and DW SE(T) specimens' initiation was followed by a rising *K*-*R* curve before reaching a peak and decreasing. The narrower SW (6.25 mm wide) specimens' *K*-*R* decline in propagation toughness occurs at a lower crack propagation distance than the wider DW (12.5 mm wide) specimens, which appears sensible given that the SW specimens' cracks had a shorter distance to grow before approaching and interacting with the back edge. Otherwise, the two different width SE(T) specimens appear to agree with one another. The shapes of the *K*-*R* curves are similar to the observations of Schwalbe and Setz in 2 mm thick M(T) specimens.[40] The peak and then decline in the *K*-*R* curves which Schwalbe and Setz observed in thicker specimens[40] was interpreted as the consequence of a transition from *K*-dominated fracture to net section yielding, and it is tempting to apply such an interpretation to our 25.4 µm thick aluminum specimens. The magnitude of *K* necessary to propagate a crack in our 25.4 µm is very low ($\approx 4\,\mathrm{MPa}\sqrt{\mathrm{m}}$) compared to thicker specimens tested by Schwalbe and Setz ($\approx 80\,\mathrm{MPa}\sqrt{\mathrm{m}}$).[40] Thus one might think that our 25.4 µm thick aluminum sheets fit nicely as an intermediate case between observations of low K_{Ic} in ultrathin FCC specimens[1–3,41] and thick sheets.[40] However, the apparent evolution of the fracture process suggested by the changing *K*-*R* curve are inconsistent with the extremely uniform fracture surfaces (Fig. 2) which lack any signs of a change in plastic zone size or crack growth mechanism. The fracture surfaces show no apparent interaction with the back edge in the fracture surfaces, nor are there any indicators that the mechanism of crack growth changed at all after the first few microns of crack growth (Fig. 2A). Additionally, the large standard deviations of the data are due to another trait of the *K*-*R* curves indicative of a similitude violation: the initiation *K* varies with starting notch length. Still, the shape of the *K*-*R* curves from Fig. 5 may appear plausible in

the context of pre-existing literature. Further analysis will show that the K results are purely an artifact of applying a LEFM analysis to a system controlled by another fracture parameter.

A comparison between SE(T) and M(T) specimens reveals a similitude violation that clear shows K cannot be a valid fracture toughness parameter for our thin aluminum sheets. If we take the K-R curves of 12.5 mm wide DW M(T) and 6.25 mm wide SW SE(T) specimens (which both have the same uncracked ligament length) and compare them, the disagreement between the specimen types becomes obvious (Fig. 6). The M(T) specimens' apparent mean initiation toughness is $2.46 \pm 0.17\,\mathrm{MPa}\sqrt{\mathrm{m}}$, which is significantly lower than the value of $3.89 \pm 0.90\,\mathrm{MPa}\sqrt{\mathrm{m}}$ computed for the SE(T) specimens. The propagation toughness as the crack length increases is also lower for the M(T) specimens than for SE(T). Neither the notch type nor the presence of anti-buckling plates influenced the initiation and propagation curves, thus the discrepancies in K are not due to out of plane deformation or notch effects. Interestingly, our J analysis does show sensitivity to this out of plane deformation, which we will discuss later along with the behavior of the fatigue precracked specimens. Linear elastic theory produces conflicting results for two specimen configurations whose crack tips should be nominally the same, yet the fracture surfaces are very consistent for all crack lengths and specimen configurations. Thus K cannot be a valid quantification of the driving force for crack growth or the local conditions around the crack tip because K fails the similitude requirement.[18]

It is worth taking a moment to discuss the meaning of the similitude comparisons made thus far in the context of "validity" criteria for crack tip parameters such as K. Standards such as ASTM E1820 dictate that a fracture toughness specimens' dimensions exceed a length based on a plastic zone size approximation based on the nominal stress intensity K_Q and yield stress σ_Y, such as $2.5(\frac{K_Q}{\sigma_Y})^2$.[24,42] If we use the 0.2 % yield stress of our 1235 aluminum specimens of 29.3 MPa (Figure 10) and initiation toughness of $3\,\mathrm{MPa}\sqrt{\mathrm{m}}$, the minimum specimen dimensions are ≈ 26.2 mm. J has a similar minimum dimension given as $10\frac{J_Q}{\sigma_Y}$ which typically allows for smaller specimens than K testing, but still imposes a lower limit on the dimensions of a J-dominated specimen.[24,27] The fact that small specimens fall below the minimum size of a standard does not, on its own,

mean that the resulting fracture toughnesses are erroneous. Validity criteria-violating specimens do, however, place a burden on the researcher to demonstrate that theory used to quantify fracture toughness is consistent with the material system. Some have argued that the elevated yield strengths observed in nanoscale FCC metal specimens[4–10,12] may reduce the minimum length scale for K or J-dominance enough to justify using LEFM or EPFM in very small ductile FCC metal fracture toughness specimens, while simultaneously using the low fracture toughness measurements to argue that the specimens were brittle.[1,2,7,10,15] However, the specimens used in our study failed by ductile crack growth (Fig. 2), produced an apparently low fracture toughness measurements (Figs. 5, 6, and 8), and at 25.4 μm are far too thick for specimen size-induced strengthening.[4–10,12] Since we are discussing specimens far smaller than the validity thresholds of J and K,[24,25,27,42] we should use the principles upon which the concept of "validity" is based, such as similitude, to determine whether or not a given fracture toughness measurement is applicable to the material system in question. We have defined similitude as the idea that the conditions near the tip of a growing crack should be nominally the same for different specimens of the same thickness of a given material, and thus there should be agreement between the fracture toughness parameters of those different specimens.[18] Similitude is the basis for standard validity criteria,[24,25] and thus a useful concept for testing the applicability of fracture toughness analysis methods at length scales well below the known valid range of a given parameter.

The elastic plastic fracture mechanics parameter J typically has a less restrictive minimum specimen size compared to K, which in principle makes J better suited for analysis for small and thin specimens. However, J approaches become intractible because out of plane deformation (buckling) influences the calculation of J from crosshead displacement-based work computations. J is defined as a path integral encompassing a crack tip $J = \int_\Gamma W dy - t \cdot \frac{\delta u}{\delta x} ds$ where Γ is the path, W is the strain energy density, y is the tensile direction, x is in-plane direction parallel to the crack, t is the traction on the path, u is the displacement, and s is the path length.[43] In practice J is computed from the force vs. crosshead displacement ($P-\Delta$) curve, consequently $J = \frac{\eta}{Bb}\int_0^\Delta P d\Delta = \frac{\eta A_{tot}}{Bb}$ where B is the specimen thickness, $b = (w-a)$ is the length of the uncracked ligament, and η

is a factor to account for specimen geometry.[43] Fig. 8 shows *J*-*R* curves computed without the geometric correction η for M(T) specimens with and without anti-buckling plates in place, which allows us to determine whether or not a J calculation is sensitive to buckling (which η would have to account for). The magnitude of the approximate J ($\approx 30\,\mathrm{kJ\,m^{-2}}$ from Fig. 8) is orders of magnitude larger than the maximum J-integral capacity of the test specimen according to ASTM E1820 ($J_{max} = \frac{B\sigma_Y}{10} = 74.4\,\mathrm{J\,m^{-2}}$ for our 25.4 µm thick sheets with a 0.2 % offset yield stress of 29.3 MPa).[24] More importantly, the $J-R$ curves in Fig. 8 show that the crosshead displacement-based J calculation is very sensitive to out of plane deformation. The anti-buckling plates used in this study restrict out of plane deformation, but do not completely suppress it. This is because anti-buckling plates pressed tightly against the specimen faces would induce friction forces to the specimen, making determination of the fracture toughness impossible. The disagreement in Fig. 8 shows that J cannot be a viable crack tip parameter until we find an alternate J measurement technique or a method to compute the η term which accounts for the effects of buckling on specimen compliance. Unlike J, the *K*-*R* curves were unaffected by the presence of anti-buckling plates (Fig. 6) because K only depends on the nominal stress and crack length. Even though K fails a test of similitude, and J's sensitivity to out-of-plane buckling complicates computation of a characteristic value of J (which very will might fail a similitude test anyway), there is a crack growth parameter which satisfies similitude tests while also being insensitive to buckling.

"Collapse analysis" (also known as limit load analysis or net section yield analysis[40,44]) reveals that the critical net section stress σ_c is a fracture toughness parameter which satisfies similitude and explains the behavior of our *K*-*R* curves. "Plastic collapse" is often disregarded in a fracture mechanics context as an extreme situation where a damage-tolerant ductile system reaches its yield stress and fails by gross plasticity before any cracks reach a large enough driving force (usually computed with K) to grow. Thus collapse analysis as a subject is mostly forgotten in the mainstream fracture mechanics community. However, one can still find some discussion of collapse in the context of the development of failure assessment diagrams (FAD) used to describe the rupture of pipes, pressure vessels, and other thin-shell structures made of especially ductile or defect-

tolerant materials.[26,45] The critical net section stress analysis used by Broek et al. can describe the driving force for crack growth in a variety of thin metal M(T) specimens in tension.[44,46] When applied to the aluminum specimens in this study, the critical net section stress criterion shows strong agreement between M(T) and SE(T) specimens of all widths, starting crack lengths, and type of notch or fatigue precrack. Fig. 7 is a plot of the nominal stress applied to all of the 1235 aluminum specimens as a function of crack length a normalized to the total specimen width w. Every specimen converges onto a single line after less than 1 mm of crack growth whether it was M(T) or SE(T), 12.5 mm wide or 6.25 mm wide, had or did not have anti-buckling plates, or had a blade-cut notch or laser-cut notch. Fatigue precracked specimens had longer initiation stages (on the order of 1 mm), but still converged to the same trend line as all of the other specimens for the remainder of crack propagation. The stress-axis intercept of the propagation trend line is the characteristic value of the collapse analysis (Fig. 7). The intercept corresponds to the critical net section stress $\sigma_c = 47\,\text{MPa}$ in the specimen and is calculated using the applied force P, thickness B, and width of the uncracked ligament ahead of the crack (i.e. the net section) $b = (w - a)$. Note that w and a represent the full width and crack length of S(T) specimens, but half of the total width and total crack length for M(T) specimens. Thus we can define the criteria for crack growth under plastic collapse in terms of the nominal stress σ for a SE(T) specimen as:

$$\sigma = \sigma_c = \frac{P}{Bb} \tag{4}$$

Similarly, the criterion for crack extension of a M(T) specimen under plastic collapse is:

$$\sigma = \sigma_c = \frac{P}{2Bb} \tag{5}$$

We computed the critical net section stress, $\sigma_c = 47\,\text{MPa}$, from the intercept of a least squares fit in *Mathematica* 10 of the critical stress of crack growth $> 125\,\mu\text{m}$ for each specimen. The first $> 125\,\mu\text{m}$ of crack growth was excluded to ensure that the trend line was only fit to the critical stress of *propagation* and exclude crack initiation. The collapse analysis in Fig. 7 shows that a

range of stable-growing cracks, whether they started from a notch or fatigue precrack, converge to the regression line from Eqns. 4 and 5 using $\sigma_c = 47\,\text{MPa}$. If we also look at the uniaxial tensile behavior of the same system (Fig. 10), we can see that the ultimate engineering tensile strength of the uniaxial specimen, $\sigma_{ult} = 49\,\text{MPa}$, is close to the intercept $\sigma_c = 47\,\text{MPa}$. This is sensible given that the uniaxial tensile strength corresponds to a specimen with an effective crack length of $a = 0$. We can demonstrate how the plastic collapse analysis fits in the context of our K and J analyses using the yield stress from the uniaxial stress-strain curve (Fig. 10). The annealed aluminum specimens are very low-strength with a 0.2 % offset yield strength of 29.3 MPa. As we discussed before, this means that our 6.25 mm to 12.5 mm wide specimens were well below the length scales for characterization with K or J. Earlier we computed the plastic zone size-based minimum specimen size for K-dominance as 26.2 mm. The minimum specimen size for J-dominance is 10.2 mm (from $10\frac{J_Q}{\sigma_Y}$ and $J \approx 30\,\text{kJ m}^{-1}$ from Fig. 8), or roughly the width of the largest specimens used in this study[24,27] Thus plastic collapse analysis is applicable to ductile systems and specimens too small for the crack tip process zone to be contained within conventional K- or J-dominated crack tip zones.

The low tensile yield strength ($\sigma_{0.2\,\%} = 29.3\,\text{MPa}$) and ductile crack growth observed are generally what would expect for the composition and microstructure of the aluminum sheets used in this study. The 1235 aluminum alloy lacks significant amounts of impurities (minimum aluminum content of 99.35 %), and has a coarse annealed microstructure (Fig. 11). The mean lineal intercept measured from 20 randomly placed and oriented lines on a micrograph of a electropolished and anodized specimen (Fig. 11) was $\bar{L} = 218\,\mu\text{m}$, which is several times the sheet thickness of 25.4 µm. The smallest grains are on the order of the sheet thickness, and the largest grains run up to 1 mm in size.

We also performed glancing angle X-ray diffraction measurements to determine the preferred orientation of grains and to check for differences between textures at the sheet surfaces. The 22 µm deep scan (in a 25.4 µm thick sheet) revealed texture consistent with the cubic (100)[001] recrystallization texture (Fig. 12 A i) observed in prior studies of rolled and recrystallized FCC metals.[47–49]

The relative volume fraction of crystals with misorientation exceeding 30° was 25.41 % for this (22 μm deep scan. The near surface textures (Fig. 12 B i) obtained for an X-ray penetration depth of 10 μm showed nominally the same texture as the full-thickness scan (Fig. 12 A i) with variation in relative crystal misorientation of 26.35 %. The similar textures at the different scan depths suggests that the texture on both sides of the sheet are nearly identical. The through-thickness texture variation observed in some thicker as-rolled aluminum sheets[50] did not manifest in our thin annealed sheets. The texture analyses and large grain size (Fig. 11) suggest any variations fracture process (Fig. 2) are most likely due to the crack encountering in-plane microstructural variations rather than through-thickness texture variation or asymmetry between the two free surfaces.

We can gain some insight into the range of crack lengths described by plastic collapse analysis use the definitions of crack growth initiation and crack propagation from ASTM B871.[34] In a displacement-controlled test, the portion of the experiment where the applied force increases is "initiation," and "propagation" is the remaining portion of the experiment where force decreases as the crack grows. This transition from initiation to propagation corresponds to the point on the nominal stress σ vs. normalized crack length a/w plot where all of the specimens tested in this study converge to the line defined by σ_c. Clearly, collapse analysis describes the propagation stage of crack growth in these thin ductile foils. The initiation stage represented less than $< 100\,\mu$m of total crack growth from both blade-cut and laser-cut notches, hence the $\Delta a > 125\,\mu$m cutoff we used to constrain our collapse analysis to include only crack propagation. The short initiation stage is also consistent with the short transition from notch to ductile fracture apparent on the fracture surfaces in Fig. 2A. If we look at the collapse analysis (Fig. 7) of the fatigue pre-cracked specimens, the initiation stage (the distance before convergence to the critical net section stress line) represents nearly 1 mm of crack growth. The fracture surfaces of the fatigue precracks (Fig. 2C) show a short transition from fatigue fracture surface to ductile tearing very much like the notch-to-tearing transition of specimens, but the length scale of the initiation stage apparent in the collapse analysis is longer (Fig. 7). The change in the initiation length scale supports the idea that the precrack eliminated the effects of notch geometry, which is why precracking is used in fracture

toughness testing. In spite of the differences in the initiation stage of the precracked specimens, crack propagation still converged to the same trend line as the notched specimens (Fig. 7). More work needs to be done to determine the full range of specimen length scales and material systems which can be characterized by σ_c-controlled crack propagation, but the present work makes the importance of distinguishing between crack growth initiation and propagation clear. While the notches and precracks used in this study altered the details of crack initiation, crack initiation represented a relatively small amount of crack growth relative to crack propagation which followed the trend line from plastic collapse analysis.

By now it should be clear that the behavior of *K*-*R* curves we commented on earlier (Figs. 5 and 6) is entirely artificial. Fig. 9 shows the relative responses of $K\left(\frac{a}{w}\right)$ when a constant critical net section stress σ_c is applied to the solutions for the various geometries used, resulting in $K = \frac{w-a}{w}\sigma_c Y\sqrt{\pi a}$. The same rising-then-falling *K*-*R* behavior observed in Figs. 5 and 6 appears in the scaling of the geometric factor shown in Fig. 9. Fig. 9 also recreates the apparent agreement between SW and DW SE(T) specimens as well as the relative magnitudes of the propagation K_R for the different specimen types. The superficially interesting *K*-*R* results are artifacts of applying LEFM to a system which is actually controlled by the collapse analysis crack growth parameter σ_c. Furthermore, the lack of an effect of the anti-buckling plates on σ_c shows that while buckling may affect the compliance of the system (and therefore our *J* calculations), it does not actually change the driving force for crack growth.

The characteristic value from collapse analysis, σ_c, is distinctly different from conventional fracture toughness crack tip parameters. *K* and *J* are typically used to describe either a single critical value of fracture toughness or the evolution of crack growth a short distance from the starting notch or precrack, i.e. they are *initiation* crack tip parameters. For brittle or high-strength materials where crack growth is unstable and sudden, such an initiation toughness measurement makes sense. Collapse analysis, on the other hand, describes the *propagation* of a crack. Stable crack propagation (which followed the $\sigma_c = 47\,\text{MPa}$ line) accounted for the majority of crack growth in the low-strength damage-tolerant thin aluminum sheets used in this study. The type of

notch or precrack altered the details of crack initiation, but collapse analysis was consistent with crack propagation for *all* of the specimens we tested.

Conclusions

Notched and fatigue precracked specimens fabricated from 25.4 μm thick 1235 aluminum were tested in tension and exhibited stable crack growth. The corresponding fracture surfaces indicated similitude between the mechanism of crack growth for both edge "SE(T)" and center "M(T)" cracked specimens of various widths. Characterization of the fracture toughness using *K*-*R* curves violated similitude between the edge notched and center-notched configurations. The evolving toughness values with crack extension shown in the *K*-*R* curves were also inconsistent with the uniformity of the fracture surfaces. By using the concept of similitude, we demonstrated that the apparently sensible*K*-*R* results were in fact artifacts of applying LEFM to ductile σ_c-controlled crack growth. We also used a *J*-*R* analysis to demonstrate that *J* is sensitive to out of plane deformation, which makes the modeling necessary to fully characterize *J* impractical. LEFM and EPFM both fail to describe crack growth in thin ductile metal sheets because *K* and *J* are crack growth initiation parameter, and crack growth in thin ductile metal sheets is predominantly crack propagation by plastic collapse.

We found that fracture of the thin ductile metal sheets used in this study was best described in terms of stable crack propagation characterized by collapse analysis. A short initiation region that was sensitive to deformation history such as fatigue precracking and notch acuity was followed by steady state tearing. This propagation stage of crack growth was described by a constant net section stress ($\sigma_c = 47\,\text{MPa}$). It is clear that thin ductile metal sheets cannot be characterized using the linear-elastic and elastic-plastic crack tip parameters *K* and *J*. Instead, crack propagation-focused plastic collapse analyses using σ_c are better suited to describing the tearing of thin ductile metal specimens.

Acknowledgments

This material is based upon work supported by the National Science Foundation under Grant No. 1609817. Any opinions, findings, and conclusions or recommendations expressed in this material are those of the authors and do not necessarily reflect the views of the National Science Foundation. The authors gratefully acknowledge the additional support of the Georgia Institute of Technology.

Bibliography

[1] Hosokawa H, Desai AV and Haque MA (2008). Plane stress fracture toughness of freestanding nanoscale thin films. *Thin Solid Films*, **516**, 6444–6447.

[2] Kumar S and Haque MA (2010). Fracture testing of nanoscale thin films inside the transmission electron microscope. *International Journal of Applied Mechanics*, **2**, 745–758.

[3] Jaya BN and Jayaram V (2016). Fracture Testing at Small-Length Scales: From Plasticity in Si to Brittleness in Pt. *JOM*, **68**, 94–108.

[4] Greer JR, Oliver WC and Nix WD (2005). Size dependence of mechanical properties of gold at the micron scale in the absence of strain gradients. *Acta Materialia*, **53**, 1821–1830.

[5] Greer JR and Nix WD (2006). Nanoscale gold pillars strengthened through dislocation starvation. *Physical Review B*, **73**, 6.

[6] Kim JY and Greer JR (2009). Tensile and compressive behavior of gold and molybdenum single crystals at the nano-scale. *Acta Materialia*, **57**, 5245–5253.

[7] Keller R, Phelps J and Read D (1996). Tensile and fracture behavior of free-standing copper films. *Materials Science and Engineering*, **214**, 42–52.

[8] Pashley D (1960). A study of the deformation and fracture of single-crystal gold films of high strength inside an electron microscope. *Proceedings of the royal society of london series a-mathematical and physical sciences*, **255**, 218–231.

[9] Espinosa H, Prorok B and Peng B (2004). Plasticity size effects in free-standing submicron polycrystalline FCC films subjected to pure tension. *Journal Of The Mechanics And Physics Of Solids*, **52**, 667–689.

[10] Hirakata H, Nishijima O, Fukuhara N, Kondo T, Yonezu A and Minoshima K (2011). Size effect on fracture toughness of freestanding copper nano-films. *Materials Science and Engineering*, **528**, 8120–8127.

[11] Ritchie RO (2011). The conflicts between strength and toughness. *Nature Materials*, **10**, 817–822.

[12] Kraft O, Gruber PA, Moenig R and Weygand D (2010). Plasticity in Confined Dimensions. In Clarke, DR and Ruhle, M and Zok, F, editor, *Annual Review of Materials Research, VOL 40*, *Annual Review of Materials Research*, volume 40, pages 293–317, Annual Reviews, 4139 El Camino Way, PO Box 10139, Palo Alto, CA 94303-0897 USA.

[13] Broberg KB (1968). Critical review of some theories in fracture mechanics. *International Journal of Fracture Mechanics*, **4**, 11–18.

[14] Steigerwald E and Hanna G (1968). Influence of work-hardening exponent on fracture toughness of high-strength materials. *Transactions Of The Metallurgical Society Of AIME*, **242**, 320–330.

[15] Kang YL, Zhang ZF, Wang HW and Qin QH (2005). Experimental investigations of the effect of thickness on fracture toughness of metallic foils. *Materials Science and Engineering: A*, **394**, 312 – 319.

[16] Zerbst U, Heinimann M, Donne CD and Steglich D (2009). Fracture and damage mechanics modelling of thin-walled structures - An overview. *Engineering Fracture Mechanics*, **76**, 5–43.

[17] Nielsen KL and Hutchinson JW (2012). Cohesive traction-separation laws for tearing of ductile metal plates. *International Journal Of Applied Mechanics*, **48**, 15–23.

[18] Ritchie R and Suresh S (1983). The fracture-mechanics similitude concept - questions concerning its application to the behavior of short fatigue cracks. *Materials Science and Engineering*, **57**, L27–L30.

[19] Anderson T (1995). *Fracture Mechanics Fundamentals and Applications*. Second edition, CRC Press, Inc.

[20] Broberg KB (1971). Crack-growth criteria and non-linear fracture mechanics. *Journal of the Mechanics and Physics of Solids*, **19**, 407–418.

[21] Cotterell B, Pardoen T and Atkins A (2005). Measuring toughness and the cohesive stress-displacement relationship by the essential work of fracture concept. *Engineering Fracture Mechanics*, **72**, 827–848, Conference on Prospects in Fracture in honor of the 65th Birthday of JG Williams, Imperial Coll London, London, ENGLAND, JUL 08-09, 2003.

[22] Haque M and Saif M (2004). Deformation mechanisms in free-standing nanoscale thin films: A quantitative in situ transmission electron microscope study. *Proceedings Of The National Academy Of Sciences Of The United States Of America*, **101**, 6335–6340.

[23] Jennings AT and Greer JR (2011). Tensile deformation of electroplated copper nanopillars. *Philosophical Magazine*, **91**, 1108–1120.

[24] ASTM International. *ASTM E1820-15a Standard Test Method for Measurement of Fracture Toughness*.

[25] McMeeking R and Parks D (1979). On criteria for j-dominance of crack-tip fields in large-scale yielding. In Landes J, Begley J and Clarke G, editors, *Elastic-Plastic Fracture, ASTM STP 668*, pages 175–194, ASTM International.

[26] McCabe D (1989). A viewpoint on the failure assessment diagram. *Nonlinear Fracture Mechanics: Volume II - Elastic-Plastic Fracture, ASTM STP*, **995**, 261–279.

[27] ASTM International. *ASTM E561-15a Standard Test Method for K-R Curve Determination*.

[28] Adair BS, Johnson WS, Antolovich SD and Staroselsky A (2013). Identification of fatigue crack growth mechanisms in IN100 superalloy as a function of temperature and frequency. *Fatigue & Fracture of Engineering Materials & Structures*, **36**, 217–227.

[29] Hahn GT and Rosenfield (1965). Local yielding and extension of a crack under plane stress. *Acta Metallurgica*, **13**, 293–306.

[30] Irwin GR (1960). Fracture mode transition for a crack traversing a plate. *Journal of Fluids Engineering*, **82**, 417–423.

[31] ASTM International. *ASTM E345-16 Standard Test Methods of Tension Testing of Metallic Foil*.

[32] Tada H, Paris P and Irwin G (2000). *The Stress Analysis of Cracks Handbook Third Edition*. ASME Press.

[33] ASTM International. *ASTM E2472-12 Standard Test Method for Determinaiton of Resistance to Stable Crack Extension under Low-Constraint Conditions*.

[34] ASTM International. *ASTM B871-01 Standard Test Method for Tear Testing of Aluminum Alloy Products*.

[35] ASTM International. *ASTM E8/E8M-16a Standard Test Methods for Tension Testing of Metallic Materials*.

[36] Vander Voort G (1984). *Metallography Principles and Practice*. McGraw-Hill, Inc.

[37] ASTM International. *ASTM E112-13 Standard Test Methods for Determining Average Grain Size*.

[38] Hutchinson JW (2014). Necking modes in multilayers and their influence on tearing toughness. *Mathematics and Mechanics of Solids*, **19**, 39–55.

[39] Kondo T, Imaoka T, Hirakata H, Sakihara M and Minoshima K (2013). Effects of stress ratio on fatigue crack propagation properties of submicron-thick free-standing copper films. *Acta Materialia*, **61**, 6310–6327.

[40] Schwalbe K and Setz W (1980). R-curves evaluation for centre cracked panels. In Radon J, editor, *Fracture and Fatigue: Elasto-Plasticity, Thin Sheet and Micromechanisms Problems*, pages 277–285, Pergamon.

[41] Meirom RA, Clark TE and Muhlstein CL (2012). The role of specimen thickness in the fracture toughness and fatigue crack growth resistance of nanocrystalline platinum films. *Acta Materialia*, **60**, 1408–1417.

[42] ASTM International. *ASTM E399-12 Standard Test Method for Linear-Elastic Plane-Strain Fracture Toughness KIc of Metallic Materials*.

[43] Zhu XK and Joyce JA (2012). Review of fracture toughness (G, K, J, CTOD, CTOA) testing and standardization. *Engineering Fracture Mechanics*, **85**, 1–46.

[44] Broek D (1986). *Elementary Engineering Fracture Mechanics*. Springer Science.

[45] Wiesner C, Maddox S, Xu W, Webster G, Burdekin F, Andrews R and Harrison J (2000). Engineering critical analyses to BS 7910 - the UK guide on methods for assessing the acceptability of flaws in metallic structures. *International Journal Of Applied Mechanics*, **77**, 883–893.

[46] Kanninen M, Broek D, Marschall C, Rybicki E, Sampath S, Simonen F and Wilkowski G, Mechanical fracture predictions for sensitized stainless steel piping with circumferential cracks.

[47] Samajdar I and Doherty RD (1998). Cube recrystallization texture in warm deformed aluminum: understanding and prediction. *Acta Materialia*, **46**, 3145–3158.

[48] Dillamore IL and Roberts WT (1965). Preferred orientation in wrought and annealed metals. *Metall. Rev.*, **10**, 271–380.

[49] Hu H (1974). Texture of metals. *Texture*, **1**, 233–258.

[50] Choi CH and Lee DN (1997). Evolution of recrystallization texture from aluminum sheet cold rolled under unlubricated condition. *Metall. Mater. Trans. A*, **28**, 2217–2222.

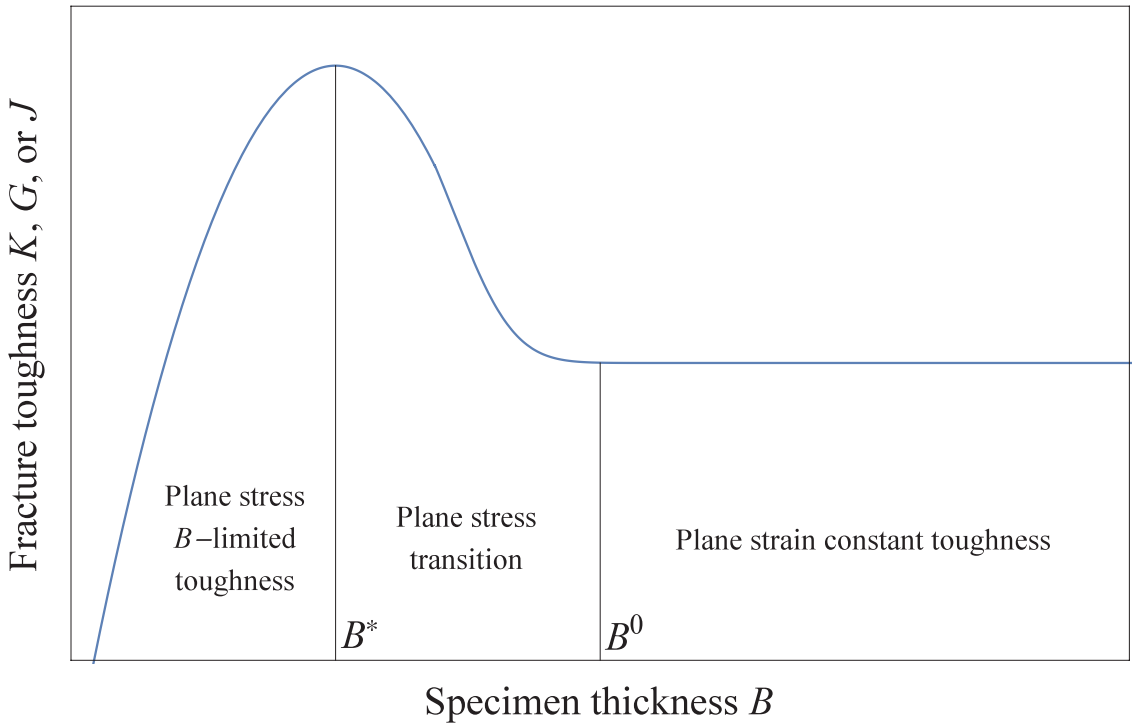

Figure 1: Schematic of the dependence of fracture toughness of metals on specimen thickness B adapted from.[14] Specimens thick enough to be predominantly in plane strain ($B > B_0$) have a constant fracture toughness.[19] At intermediate thicknesses ($B^* < B < B_0$) the transition from plane strain to plane stress with decreasing thickness corresponds to an increase in fracture toughness. Below a certain critical thickness (B^*) and maximum fracture toughness, fracture toughness is thickness-limited and decreases with B.[20]

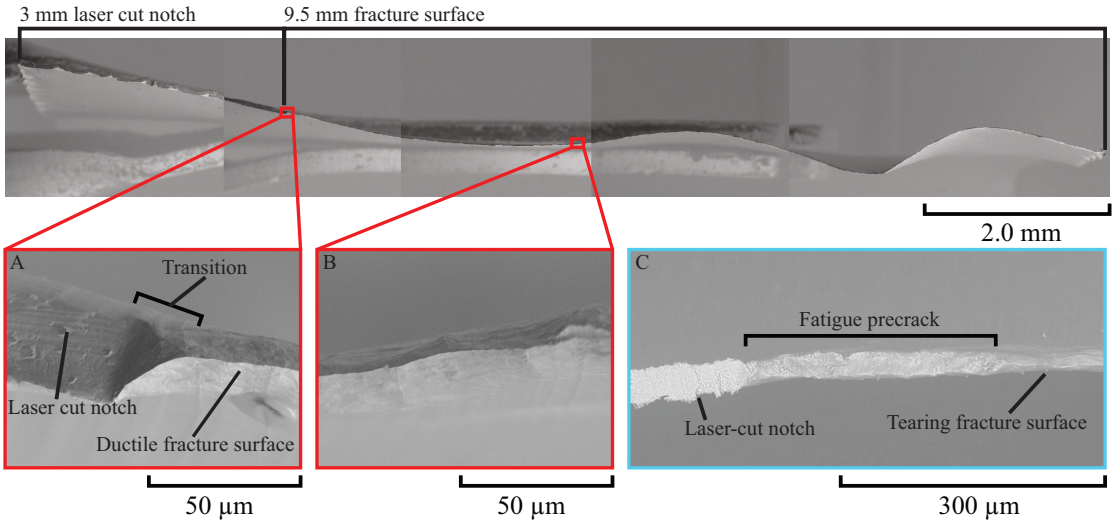

Figure 2: Representative SEM micrographs of the fracture surface of a double wide (DW) specimen. Beyond a short initiation region ('A' at left) near the 3 mm laser-cut notch, the fracture surface along the entire width of the specimen is uniform ('B' in center). All regions of the fracture surface show ductile fracture with reduction in thickness (necking) down to a sharp point before final separation. Also inset is the fracture surface of a fatigue pre-cracked specimen ('C' at lower right). While notches and fatigue precracks have distinctly different surfaces ('A' and 'C'), all of the fracture are visually similar and indicative of a transverse neck down to separation ('B').

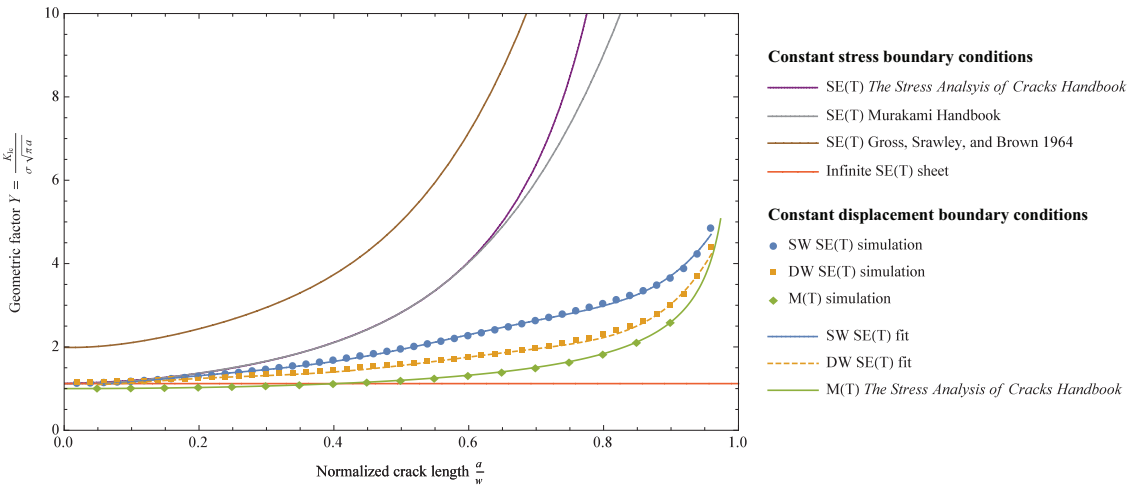

Figure 3: Plot of the geometric term Y from the LEFM stress intensity factor $K = Y\sqrt{\pi a}$ from our FE simulations and various handbook solutions. Markers show the output from the FE simulations and lines show our fits to the SE(T) solutions and the solution from The Stress Analysis of Cracks Handbook which agrees with the M(T) simulations.[32] Our SE(T) solutions and the handbook SE(T) solutions differ because the handbook solutions were computed for constant stress boundary conditions with the specimen ends left free to rotate. (The Gross solution offset is possibly due to a typographical error in[1]). Our solutions from finite element used constant displacement boundary conditions with the ends held fixed, which is consistent with specimens prevented from rotating by rotationally rigid test fixture grips.[1,2,10,39] Running the same FEA simulations with constant stress boundary conditions and the specimen ends free to rotate reproduces the geometric factor from The Stress Analysis of Cracks Handbook within 1 % for all $\frac{a}{W}$.[32]

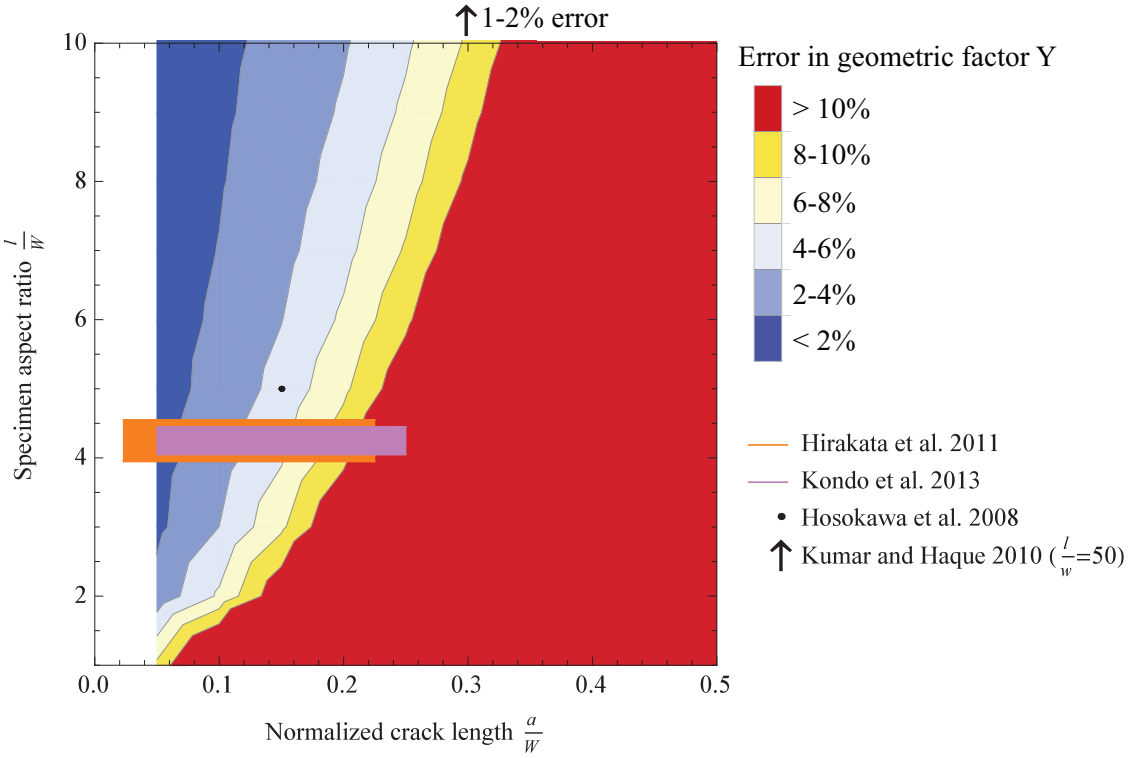

Figure 4: Contour plot of the % error introduced to a K measurement in a SE(T) specimen due to assuming that the specimen ends are free to rotate when they are actually fixed. Overlaid are some examples of SE(T) experiments from the literature which treated SE(T) specimens with fixed ends as being able to freely rotate (see Figure 4).[1,2,10,39] The error increases with decreasing aspect ratio and increasing crack length.

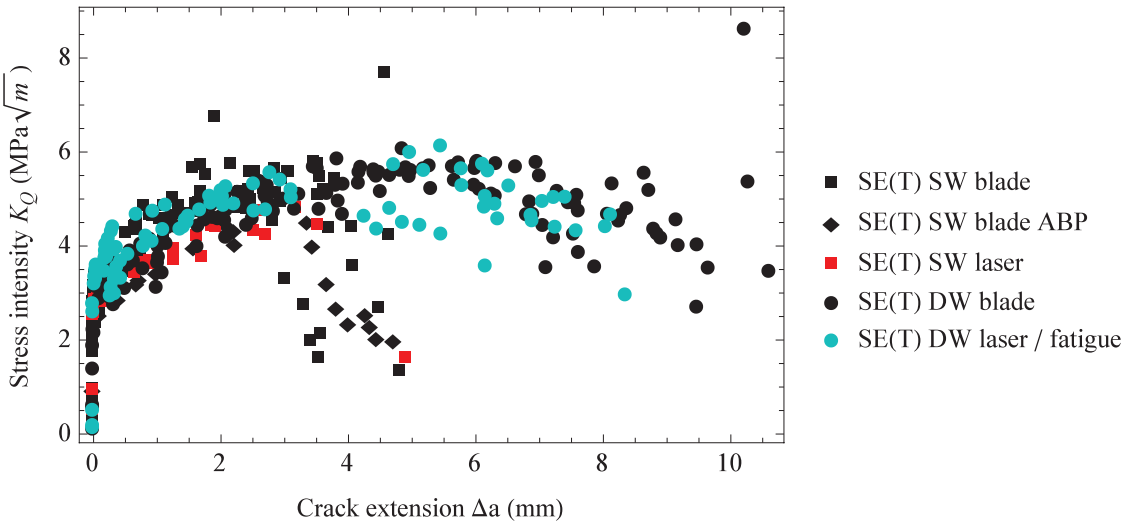

Figure 5: K-R curves from 6.25 mm wide (SW) and 12.5 mm wide (DW) 25.4 µm thick single edge notch tension "SE(T)" specimens. The two types of specimen exhibited nominally the same initial rising R behavior, but the peaks and declines of R in the wider specimens occur at longer crack lengths.

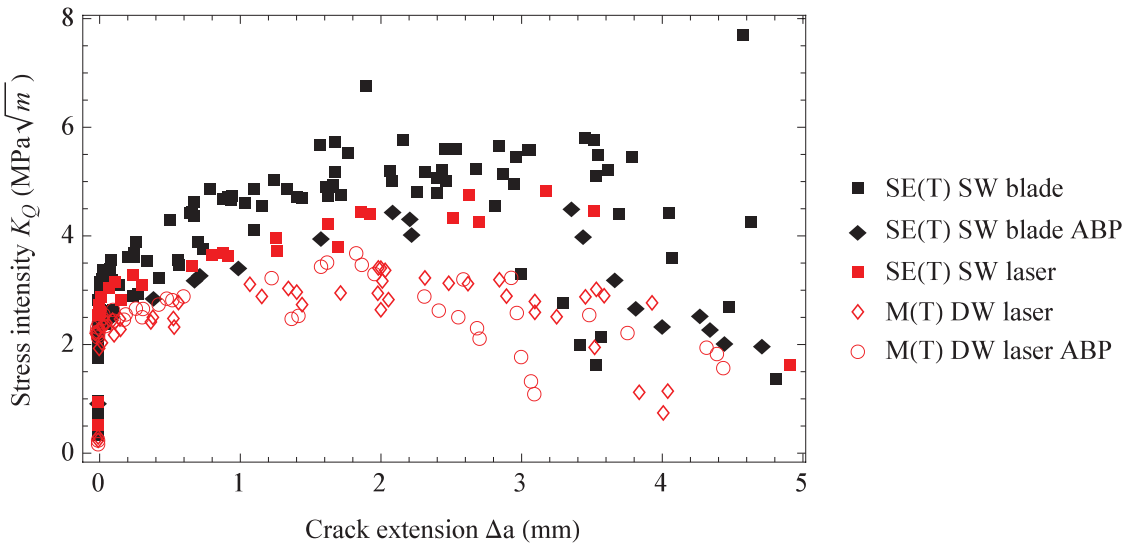

Figure 6: K-R curves from $W = 6.25\,\text{mm}$ wide (SW) single edge notch tensile "SE(T)" and $2W = 12.5\,\text{mm}$ wide (DW) middle notch tension "M(T)" specimens. The two types of specimen were of nominally the same geometry in terms of net section length $(w-a)$, but the peak stress intensity reached by the CNT specimens was notably lower than that of the SE(T) specimens.

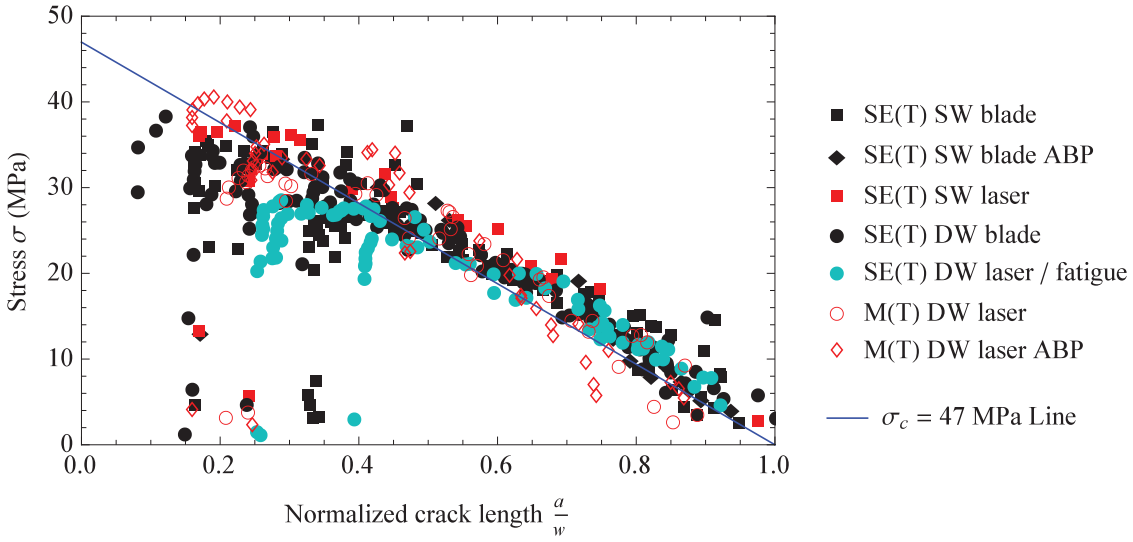

Figure 7: Stress as a function of crack length normalized to specimen width $\frac{a}{W}$. The linear decrease of σ_c to zero as a approaches W is consistent with crack growth controlled by the effective stress in the net section, shown here as a line for $\sigma_c = 47\,\text{MPa}$. Regardless of specimen type, the nominal stress rises without crack growth until reaching the $\sigma_c = 47\,\text{MPa}$ line, then crack growth proceeds as the nominal stress decreases to follow the $\sigma_c = 47\,\text{MPa}$ line. Note that w and a represent the full width and crack length of S(T) specimens, but half of the total width and total crack length for M(T) specimens.

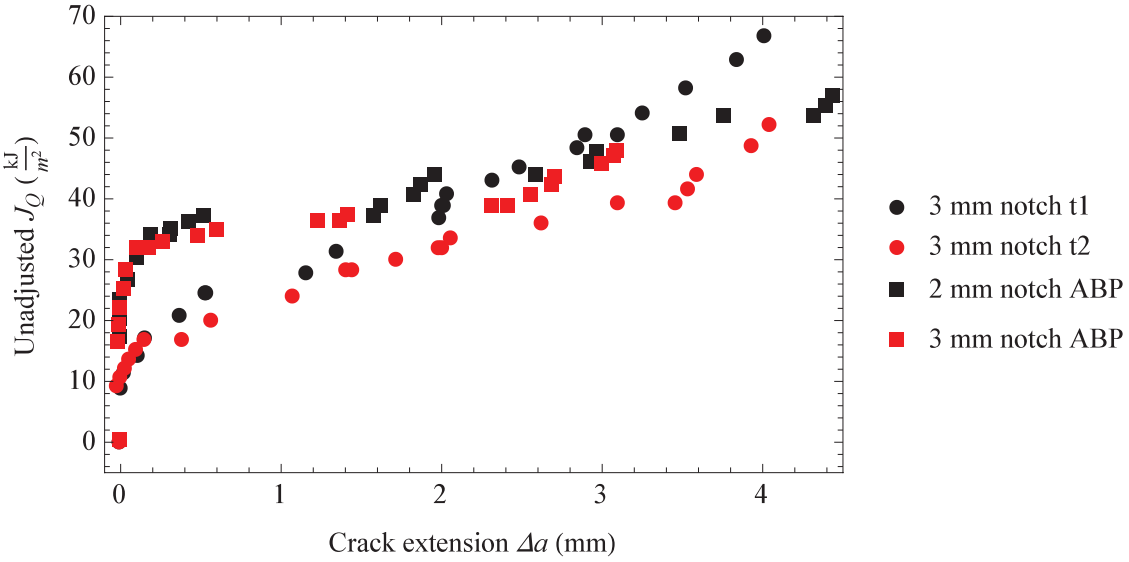

Figure 8: *J-R* curves for M(T) specimens with and without anti-buckling plates (denoted as "ABP"). These were computed without the geometric correction η, but still allow us to compare the effects of the anti-buckling plates. The disagreement between the curves indicates a high degree of sensitivity of crosshead displacement-based J to out of plane deformation.

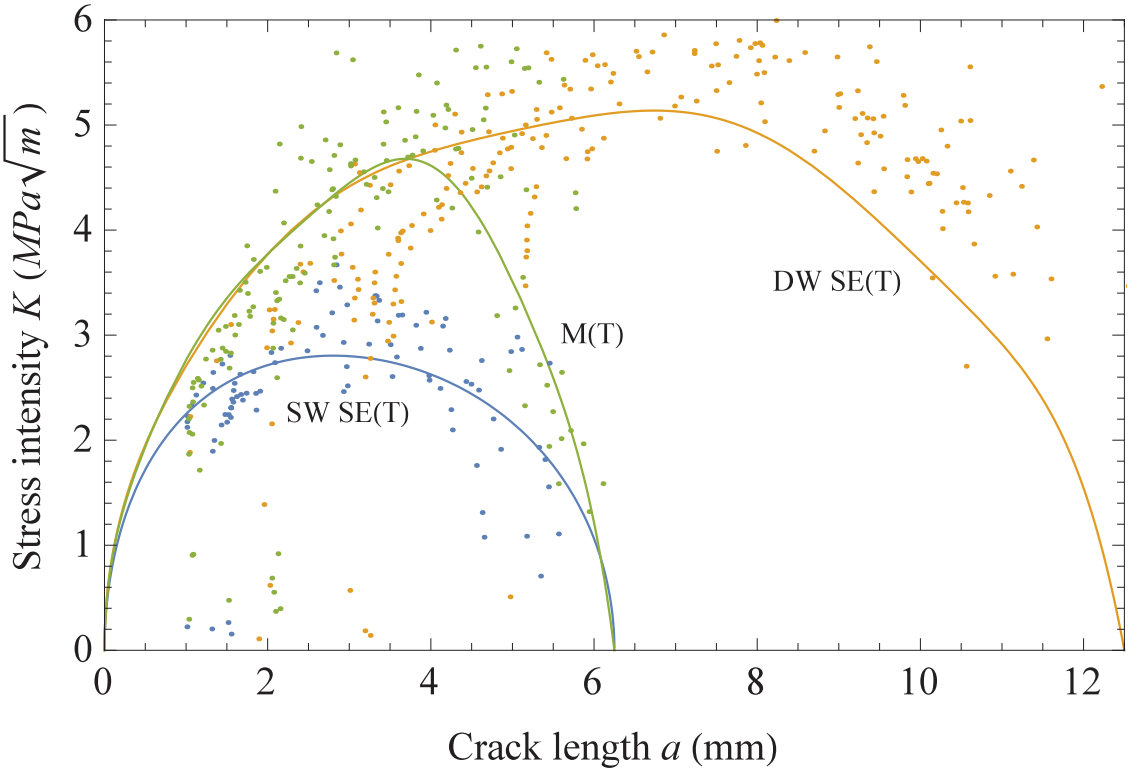

Figure 9: Predicted *K-R* curves demonstrating the apparent *K-R* curves of specimens with crack growth controlled by the constant net section stress $\sigma_c = 47\,\text{MPa}$ measured by extrapolating the critical stresses shown in Fig. 7 to $\frac{a}{W} = 0$. The results closely match the experimentally measured *K-R* curves (Figs. 5 and 6). Note the coinciding SW and DW curves at short crack lengths which would give the *appearance* of similitude between the two different widths of SE(T) specimen at short crack lengths.

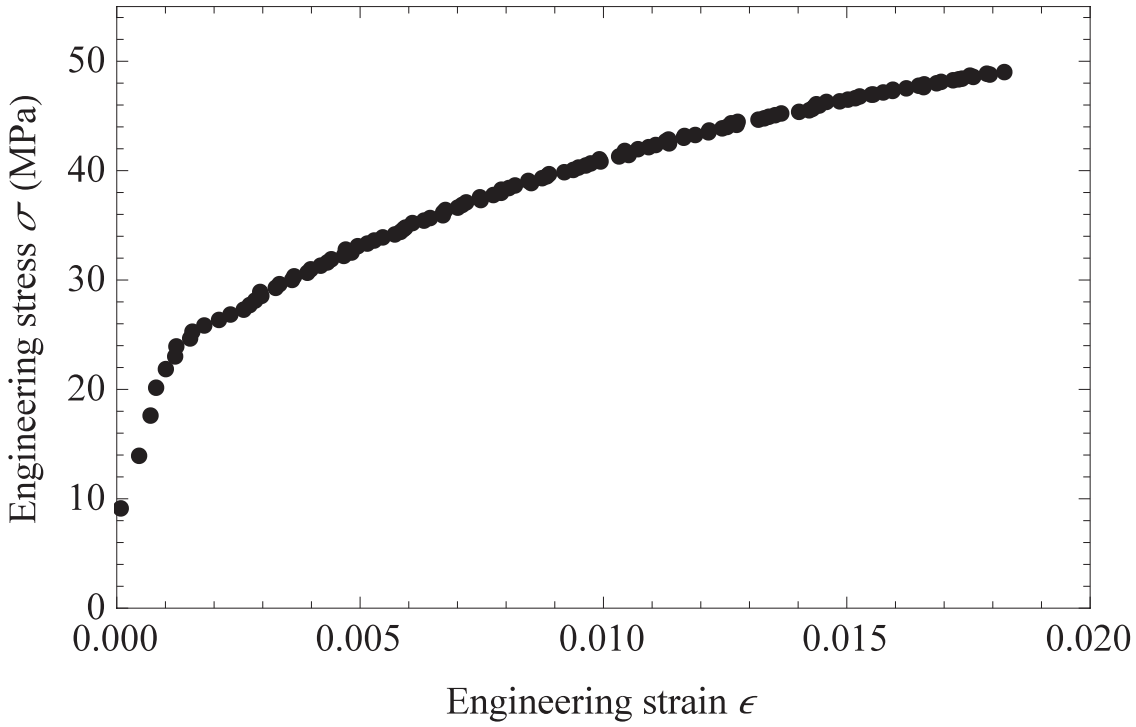

Figure 10: Engineering stress-strain curve from an un-notched DW specimen.

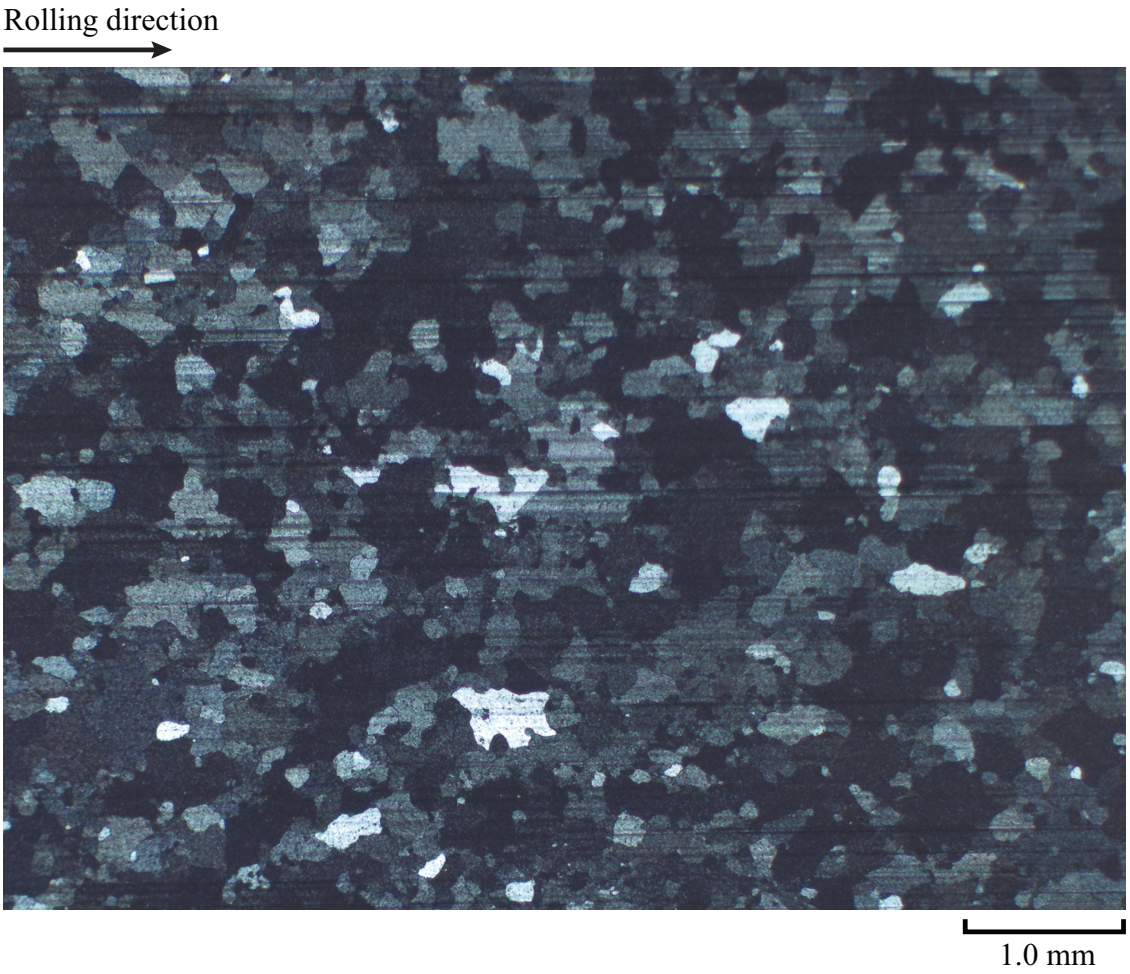

Figure 11: Bright field polarized light optical micrograph of an electropolished and annealed anodized sheet. The thin surface oxide layer gives contrast to the underlying grains when imaged with polarized light. Some of the deeper marks from the original rolled surface finish are visible through the oxide. This micrograph was used with 20 randomly located and oriented lines to compute the mean lineal intercept grain size $\bar{L} = 218\,\mu\text{m}$.

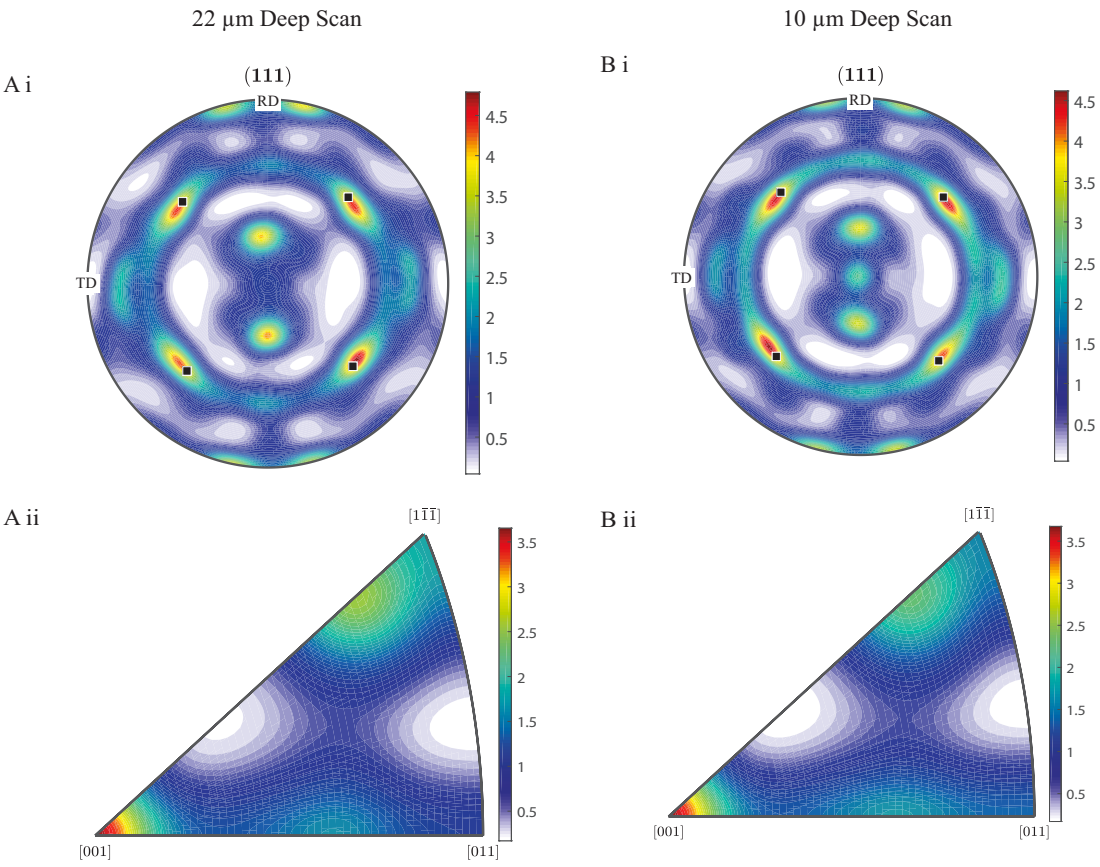

Figure 12: [111] pole figures (A i and B i) and normal direction (ND) inverse pole figures (A ii and B ii) from 22 µm (A i and A ii) and 10 µm (B i and B ii) deep glancing angle X-ray diffraction scans. The pole figures (A i and B i) are ND projections with the rolling direction (RD) aligned to the vertical (x) axis and the transverse direction (TD) aligned to the horizontal(y) axis.